Lawrence Berkeley National Laboratory

Title
NEAR-IR TWO PHOTON MICROSCOPY IMAGING OF SILICA NANOPARTICLES FUNCTIONALIZED WITH ISOLATED SENSITIZED Yb(III) CENTERS

Permalink
https://escholarship.org/uc/item/5pb6h293

Authors
Lapadula, Giuseppe
Bourdolle, Adrien
Allouche, Florian
et al.

Publication Date
2014

NEAR-IR TWO PHOTON MICROSCOPY IMAGING OF SILICA NANOPARTICLES FUNCTIONALIZED WITH ISOLATED SENSITIZED Yb(III) CENTERS.

Giuseppe Lapadula,[1] Adrien Bourdolle,[2,3] Florian Allouche,[1] Matthew P. Conley,[1] Iker del Rosal,[4] Laurent Maron,[4] Wayne W. Lukens,[5] Yannick Guyot,[6] Chantal Andraud,[2] Sophie Brasselet,[7] Christophe Copéret,[1#,3*] Olivier Maury,[2*] Richard A. Andersen.[8]

[1] ETH Zürich, Department of Chemistry and Applied Biosciences, Vladimir Prelog Weg 2, CH–8093 Zürich, Switzerland

[2] Université de Lyon, CNRS, UMR 5182–CNRS – Ecole Normale Supérieure de Lyon, Universtité de Lyon 1, 46 allée d'Italie, 69007 Lyon, France

[3] Université de Lyon, C2P2, UMR 5265 (CNRS–CPE Lyon–Université Lyon 1), 43 Bd. Du 11 Novembre 1918, 69616 Ville-urbanne Cedex, France

[4] Université de Toulouse and CNRS, LPCNO INSA/UPS/CNRS 135, avenue de Rangueil – 31077 Toulouse Cedex 4, France

[5] Chemical Sciences Division, University of California, Lawrence Berkeley National Laboratory, Berkeley, CA 94720 (USA)

[6] Université de Lyon, , Institut Lumière Matière, UMR 5306 CNRS–Université Lyon1, 10 rue Ada Byron, 69622 Villeurbanne Cedex, France

[7] Institut Fresnel, CNRS UMR 6133, Université Aix Marseille III, Ecole Centrale de Marseille, Domaine Universitaire St Jérome, 13397 Marseille Cedex 20, France

[8] Department of Chemistry, University of California, Berkeley, CA 94720, USA

ABSTRACT: Bright nano objects emitting in the near infrared with a maximal cross section of 41.4 x 10 GM (Goppert Mayer), were prepared by implanting ca. 180 4,4'–diethylaminostyryl–2,2'–bipyridine (DEAS) Yb(III) complexes on the surface of 12–nm silica nanoparticles. The surface complexes ([DEAS•Ln@SiO], Ln =Y,Yb) were characterized using IR, solid–state NMR, UV–Vis, EXAFS spectroscopies in combination with the preparation and characterization of similar molecular analogues by analytical techniques (IR, solution NMR, UV–Vis, X ray crystallography) as well as DFT calculations. Starting from the partial dehydroxylation of the silica at 700 °C on high vacuum having 0.8 $OH.nm^{-2}$, the grafting of $Ln(N(SiMe))$ generate $\equiv SiO–Ln(N(SiMe))$, which upon thermal step and coordination of the DEAS chromophore yields $(\equiv SiO)Ln(DEAS)$. Surface and molecular analogues display similar properties, in terms of DEAS binding constants absorption maxima and luminescence properties (intense emission band assigned to a ligand centered CT fluorescence and life time) in the solid state, consistent with the molecular nature of the surface species. The densely functionalized nanoparticles can be dispersed via ultra-sonication in small *ca.* 15-20 nm aggregates (1 to 6 elementary particles) that were detected using two–photon microscopy imaging at 720 nm excitation, making them promising nano–objects for bio–imaging.

1 Introduction

The need for effective chemical sensors that could be useful for imaging biological samples *in vitro* or *in vivo* has been one of the major driving forces for the development of luminescent molecules and materials.[ ] While many examples of strongly luminescent molecules for chemical sensing in biological samples are currently available,[ ] the excitation wavelength lies in most cases in the visible region of the spectrum, which does not deeply penetrate biological tissues and can lead to a potential risk for photo–damage because of the high energy of visible light.[ ] One potential solution to these challenges is the use of near infrared (NIR) light, located in the 700–1200 nm spectral range, because biological tissues are effectively transparent in this region leading to less scattering.[ ] Though attractive, most chromophores are not fully optimized for this spectral range (low quantum yield, small Stokes Shift).[ ] Biphotonic microscopy

would give the benefits of NIR excitation with desirable luminescent properties.[ ] Biphotonic microscopy relies on the nonlinear simultaneous absorption of two photons of half energy in the NIR, from an intense femtosecond Ti:sapphire laser source [700–1050 nm][ ] which enables the use of chromophores that are excited in the visible region with NIR light. However, most chromophores designed for biphotonic microscopy emit at higher energy compared to the laser excitation and fall in the visible region. Only a few notable examples of red emitters have been reported.[ ] Ytterbium complexes are ideal candidates for NIR–to–NIR biphotonic microscopy because of the $^2F_{5/2} \rightarrow {}^2F_{7/2}$ ytterbium (III) transition around 1000 nm, an emission at higher wavelength than the incident laser.[ ] This emission has been used for 3D imaging of a mouse brain vascular network.[ ] Though promising, the low luminescent quantum yield

efficiency of molecular ytterbium species limits the generality of this technique.[■]

To overcome this drawback the two–photon brightness parameter – defined as the product of the two–photon cross–section and the quantum yield – can be improved using the *local concentration effect,* i.e., the confinement of a large number of chromophores in a nanoscale size object. This strategy has been successfully used for organic chromophores and europium based luminescent single nanoparticles.[■-■] Though these nano–materials offer potentially intriguing luminescence properties, detrimental luminescent self–quenching may occur in some doped luminescent nanoparticles prepared by Stöber or ORMOSIL (Organically Modified Silica) emulsion sol–gel techniques. Here we describe the preparation and molecular–level characterization of bright ytterbium–containing luminescent nanoparticles (LSN). We use Surface Organo Metallic Chemistry (SOMC)[■-■] to regularly position well–defined chromophoric ytterbium complexes containing DEAS = 4,4'–diethylaminostyryl–2,2'–bipyridine, a nonlinear optical chromophore–ligand[■-■] on the silica surface. These Yb–based LSN's were detected using NIR–to–NIR biphotonic optical microscopy.[■]

The direct characterization of these materials by spectroscopic methods was complemented by characterizing the corresponding diamagnetic yttrium analogous surface species and homogeneous molecular siloxide analogues Ln(OSi(OtBu))$_x$(L) (Ln = Y and Yb with L = 4,4'–Me$_2$bipy and DEAS). The photophysical properties of the surface complexes are comparable to the molecular complexes, clearly showing that the surface species are located in a well–defined molecular environment. These results allow direct structure – property relationship between a structure of the functionalized nanoparticles and the photophysical properties.
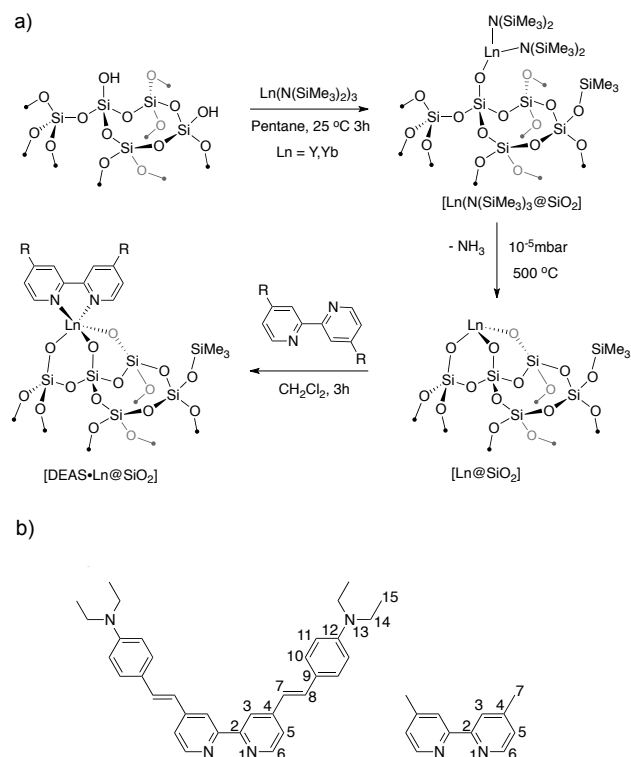
2 Results and Discussion

The synthesis of silica particles functionalized with chromophores bound to surface Ln isolated site is performed in a three–step procedure as shown in Scheme 1. The silica nanoparticles pre–treated at 700 °C under vacuum, having a low density of surface silanols ([SiO$_{2-700}$], 0.8 OH.nm^{-2}, 0.26 mmol/g), are contacted with Ln(N(SiMe$_3$)$_3$)$_3$ (Ln = Y and Yb) yielding [Ln(N(SiMe$_3$)$_3$@SiO$_2$]. The materials were heated at 500 C for 12h under high vacuum to give [Ln@SiO$_2$], and were subsequently contacted with 4,4'–diethylaminostyryl–2,2'–bipyridine (DEAS), to yield [DEAS•Ln@SiO$_2$].

Scheme 1: a) Grafting of Ln(N(SiMe)$_3$)$_3$ on SiO$_{2-700}$ to give [Ln(N(SiMe)$_3$)$_3$@SiO$_2$], thermal treatment to give the tripodal species and coordination of the bipy ligand b): DEAS ligand (left), 4,4'–Me$_2$bipy (right), in both species the carbon and nitrogen atoms are labeled.

2.1 Synthesis and characterization of surface species.

Silica functionalization – [Ln(N(SiMe)$_3$)$_3$@SiO$_2$]. The reaction of Y(N(SiMe)$_3$)$_3$ with [SiO$_2$] in pentane yields the off–white solid [Y(N(SiMe)$_3$)$_3$@SiO$_2$]. The infrared spectrum of [Y(N(SiMe)$_3$)$_3$@SiO$_2$] (Figure S1A) lacks a strong silanol vibration and contains ν$_{CH}$ bands at 2951 and 2900 cm^{-1} and a shoulder at 2820 cm^{-1}, attributed to the SiMe$_3$ groups from ≡SiO–Y(N(SiMe)$_3$)$_2$ and ≡SiO–SiMe$_3$ surface species (eq. 1–2). The ≡SiO–SiMe$_3$ surface species results from the formation of HN(SiMe)$_3$)$_2$ (eq. 1) and the subsequent competitive reaction with silanols (eq. 2).[■,■]

Ln(N(SiMe)$_3$)$_3$ + ≡SiO–H → (Me$_3$Si)$_2$NH + ≡SiO–Ln(N(SiMe)$_3$)$_2$ (1)

(Me$_3$Si)$_2$N–H + 2 ≡SiO–H → NH$_3$ + 2 ≡SiO–SiMe$_3$ (2)

Table 1: Ln, C and N Elemental analysis of Y and Yb–based materials after grafting, post–treatment and reaction with DEAS.

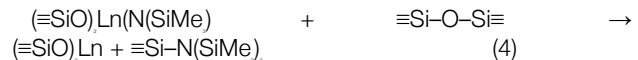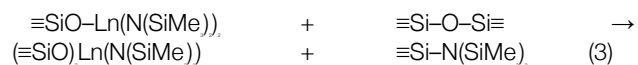| Entry	Materials	Element Loading (wt%)			Ratio	
		Ln	C	N	C/Ln	N/Ln
1	[Y(N(SiMe$_3$)$_3$)@SiO$_2$]	1.83	3.64	0.64	15 ± 1	2 ± 1
2	[Yb(N(SiMe$_3$)$_3$)@SiO$_2$]	3.95	3.55	0.76	15 ± 1	2 ± 1
3	[Y@SiO$_2$]	2.10	1.36	0.42	5 ± 1	0.5 ± 1
4	[Yb@SiO$_2$]	4.14	1.58	0.31	5 ± 1	0.5 ± 1
5	[DEAS•Y@SiO$_2$]	2.05	4.72	1.01	14.5 ± 1	1.9 ± 1
6	[DEAS•Yb@SiO$_2$]	3.95	4.72	0.99	14.5 ± 1	1.9 ± 1

The IR spectrum also contains low intensity bands in the 3464 and 3534 cm^{-1} region that are associated with N–H vibrations, which can be attributed to strongly adsorbed compounds such as (Me$_3$Si)$_x$N(H)$_{3-x}$ (0 < x ≤ 3), generated

upon reaction of Y(N(SiMe)) with surface silanols (eq. 1). The IR spectrum of [Yb(N(SiMe))@SiO] shows very similar features to those of [Y(N(SiMe))@SiO]; (Figure S1B).

[Y(N(SiMe))@SiO] contains 1.83 %$_{wt}$ Y according to elemental analysis, which corresponds to 0.21 mmol Y/g of silica (Table 1, Entry 1). This value is slightly lower than expected for quantitative grafting (0.26 mmol SiOH/g for [SiO$_{1000}$]), consistent with the competitive reaction of HN(SiMe)$_3$ with silanols. Elemental analyses for carbon (3.64 %$_{wt}$) and nitrogen (0.64 %$_{wt}$) indicate that 15 ± 1 C and 2 ± 1 N are still present per Y atom, which is consistent with the presence of ≡SiO–Y(N(SiMe))$_2$ (2 N per Y and 12 C per Y) along with minor amounts of ≡SiO–SiMe$_3$ (ca. 0.05 mmol. per g – 20% of the silanol sites). [Yb(N(SiMe))@SiO] affords similar analytical data: 3.95 %$_{wt}$ Yb, 3.55 %$_{wt}$ C and 0.76 %$_{wt}$ N (15 C and 2 N per Yb), which corresponds to 0.21 mmol ≡SiO–Yb(N(SiMe))$_2$ g^{-1} along with 0.05 mmol.g^{-1} of ≡SiO–SiMe$_3$ (Table 1, Entry 2). The elemental analysis data indicate that *ca.* 360 Ln units are present per 12 nm silica particle. [Y(N(SiMe))@SiO] was also characterized by solid state NMR. The Magic Angle Spinning (MAS) ^{1}H NMR spectrum contains a signal centered at 0 ppm and a lower intensity resonance at 0.44 ppm assigned to the grafted ≡SiO–Y(N(SiMe))$_2$ and ≡SiO–SiMe$_3$ respectively, along with an extra peak at 0.87 ppm that is assigned to the adsorbed (Me$_3$Si)$_2$N(H) (Figure S2). The carbon–13 Cross–Polarization Magic Angle Spinning (CPMAS) NMR spectrum shows only one peak centered at 1 ppm, which can be assigned to the Me$_3$Si fragment of both ≡SiO–Y(N(SiMe))$_2$ and ≡SiO–SiMe$_3$ surface species. The ^{29}Si CPMAS spectrum shows the expected peaks at –92 ppm and –101 ppm corresponding to Q$_3$ and Q$_4$ sites of silica,^{xx} and three peaks at –11, 5 and 16 ppm which are assigned to Y–N(*Si*Me)$_{2x}$, (Me*Si*)$_2$N(H), and O*Si*Me$_3$, respectively.

Stabilizing thermal treatment – Generation of [Ln@SiO]. Treatment of [Ln(N(SiMe))@SiO] at high temperatures (500 °C) under vacuum (10^{-5} mbar) results in a sharp decrease in intensity of the ν(CH) bands at 2951 and 2900 cm^{-1} after 8 h. Note that a ν$_{xx}$ signal is not regenerated during this process, but the ≡SiO–SiMe$_3$ surface species are still present as evidenced by the remaining C–H vibrations at 2963 and 2905 cm^{-1} (Figures S1A and S3). Elemental analysis of [Y@SiO] gives 2.10 %$_{wt}$ Y, 1.36 %$_{wt}$ C, and 0.42 %$_{wt}$ N, consistent with a constant amount of Y and a loss of most organic functionalities (Table 1, Entry 3). The absolute fate of the silylamide during this treatment remains unknown, but elemental analysis shows that most of carbon and nitrogen are eliminated in [Y@SiO], albeit small quantities of carbon and nitrogen persist (5 C/Ln and 0.5 N/Ln). Characterization of [Y@SiO] by solid–state NMR shows that most surface organic functionalities have disappeared, and that only ≡SiO–SiMe$_3$ groups remain at the surface as evidenced by the presence of a single peak in the ^{1}H MAS spectrum at 0.05 ppm, and the resonance at 0.0 ppm in the ^{13}C CP–MAS NMR spectrum (Figure S4). It is likely that during the thermal treatment the –N(SiMe)$_2$ fragment is transferred to the surface by opening an adjacent siloxane bridge, thus forming new Y–O bonds and ≡Si–N(SiMe)$_2$ (eq. 3–4),^{xx} the latter presumably further decomposing into SiNH$_x$ surface species.^{xx} Similar observations are obtained for the thermal treatment of the [Yb(N(SiMe))@SiO] to form [Yb@SiO], albeit at a slightly lower decomposition temperature (Figure S3). Ele-

mental analysis of [Yb@SiO] gives 4.14 %$_{wt}$ Y, 1.58 %wt C, 0.31 %$_{wt}$ N (Table 1, Entry 4).

≡SiO–Ln(N(SiMe))$_2$ + ≡Si–O–Si≡ → (≡SiO)$_2$Ln(N(SiMe))$_2$ + ≡Si–N(SiMe)$_2$ (3)

(≡SiO)$_2$Ln(N(SiMe)$_2$ + ≡Si–O–Si≡ → (≡SiO)$_3$Ln + ≡Si–N(SiMe)$_2$ (4)

We characterized the [Ln@SiO] materials by Extended X–Ray Absorption Fine Structure (EXAFS) analysis (Table 2 and Figure S5). For [Y@SiO], the EXAFS data are consistent with a yttrium atom surrounded by three oxygen atoms at short distance of 2.221(8) Å, and two additional O neighbors at 2.40(1) Å. These values indicate that the yttrium atom is bonded to three oxygen atoms, and also coordinated to nearby siloxane bridges, (≡SiO)$_3$Y(≡SiOSi≡). For [Yb@SiO], the Yb ion is also surrounded by three oxygen atoms at short distances (2.11(2) Å), but interacts with more siloxane bridges at longer distances, (≡SiO)$_3$Yb(≡SiOSi≡)$_2$. It should be noted that coordination numbers determined by EXAFS are strongly correlated with the thermal Debye–Waller factor (σ), which results in large uncertainties. In the case of [Ln@SiO], this effect is most pronounced for the second oxygen atom shell, which are presumably siloxane bridges. Because of the uncertainty in the coordination numbers, there may be little actual difference between the coordination environment of [Yb@SiO] and [Y@SiO] other than the M–O bond distances, which are slightly shorter for Yb than for Y.

Table 2: Fitted EXAFS data for [Y@SiO] and [Yb@SiO]

	[Y@SiO]	[Yb@SiO]
ΔE (eV)	2(1)	4(2)
S$_0$	0.9	0.9
Neighbor (#)	O (3)	O (3)
	O^a (2)	O^a(4)
Distance Ln–O (Å)	2.211	2.11
Distance Ln–O^a (Å)	2.40	2.30
σ^2 Ln–O(Å)	0.0051(6)	0.009(2)
σ^{2a} Ln–O(Å)	0.0036(9)	0.013(3)
p^b Ln–O	<0.001	0.01
p^b Ln–O^a	<0.001	0.002

a) second oxygen neighbor. b) Probability that the improvement to the fit due to adding this set of atoms is due to random error. A p < 0.01 means that the improvement to the fit is better than 3 standard deviation.

Coordination of DEAS to [Ln@SiO] – Formation of [DEAS•Ln@SiO]. Contacting the off–white [Ln@SiO] with a yellow solution of DEAS in CH$_2$Cl$_2$ results in a fast discoloration of the supernatant and yields [DEAS•Ln@SiO] as deep red solids (Scheme 1 and eq 5).

(≡SiO)$_3$Ln+ DEAS → [DEAS•Ln@SiO] (5)

The IR spectrum is almost identical for both lanthanides: the orange–red [DEAS•Y@SiO] and deep–red [DEAS•Yb@SiO] contains new bands associated with DEAS. In particular the two bands at 1522 and 1586 cm⁻¹ attributed to ν(C=C) are blue–shifted by 15 cm⁻¹ with respect to free DEAS, evidence for coordination of DEAS to the metal center (Figures S6).[x] The same shift is observed in model molecular complexes Ln(OSi(O*t*Bu)₃)₃(DEAS) (*vide infra*). Elemental analysis of [DEAS•Y@SiO] gives 2.05 %_w Y, 4.72 %_w C and 1.01 %_w N (Table 1, Entry 5). With respect to [Y@SiO], the nitrogen and carbon contents increase from 0.38 to 1.01 %_w and 1.36 to 4.72 %_w, respectively, which corresponds to an increase of 1.9 ± 1 N and 14.5 ± 1 C per Y atom. For [DEAS•Yb@SiO], elemental analyses (3.95 %_w Yb, 0.99 %_w N and 4.72 %_w C) also show a similar increase of 2 ± 1 N and 14.5 ± 1 C per Yb (Table 1, Entry 6). Since DEAS contains 28 C and 4 N atoms, these increases are consistent with the coordination of DEAS to ca. 50% of the Ln sites. From this data we can conclude that the particles contain *ca.* 180 DEAS•Ln fragments per 12 nm particle. The non–complete coordination of all the lanthanide centers (ca. 1 Ln.nm⁻²) is likely due to the size of DEAS ligand. The projected area of DEAS is ca. 2 nm², large enough that a silica nanoparticle cannot accommodate more than 0.5 DEAS.nm⁻². Similar behavior was observed for [DEAS•Zn@SiO].[x]

The ¹H solid–state NMR spectrum of [DEAS•Y@SiO] displays additional signals at 7.0 (CH₃), 3.2 (NCH₂CH₃), and 0.94 (NCH₂CH₃), consistent with the presence of DEAS. The ¹³C CP–MAS solid–state NMR spectrum show typical peaks associated with the coordination of DEAS to Y as evidenced by the downfield shift of the methine carbon in alpha of the pyridine nitrogen (carbon– 6 in Scheme 1b, Figure S7) from 155 ppm in free DEAS to 158 ppm in [DEAS•Y@SiO].[x] For [DEAS•Yb@SiO], solid–state NMR analyses were not performed because of the paramagnetic Yb center.

2.2 Molecular and Computational Models.

The synthesis and the characterization of molecular analogues of the surface species generally results in a deeper understanding of the surface species.[xx] HOSi(O*t*Bu)₃ is a useful model of an isolated silanol since the silicon is surrounded by four oxygen atoms, as in silica, three of which are –O*t*Bu groups and one is the –OH reactive site.[x] Additionally, HOSi(O*t*Bu)₃ can also accommodate secondary interactions between the metal center and the oxygen of the O*t*Bu groups.[x] Since the –O*t*Bu ligands are rather bulky, monomeric lanthanide siloxides are expected and would serve as good models for the silica surface. The targeted molecular model complexes are Ln(OSi(O*t*Bu)₃)₃(DEAS). We also synthesized the Ln(OSi(O*t*Bu)₃)₃(4,4'–Me₂bipy) for diffraction studies due to the reluctance of DEAS–metal complexes to form X–Ray quality crystals.

Addition of 4 equiv. of HOSi(O*t*Bu)₃ to Ln(N(SiMe₃)₂)₃ in CH₂Cl₂ gives Ln(OSi(O*t*Bu)₃)₃(η–HOSi(O*t*Bu)₃) in good yields (Ln = Y, 75 %; Ln = Yb, 72 %; Scheme 2). For Y and Yb, the isolated siloxides crystallize with an additional molecule of silanol, which accounts for the stoichiometry of the reaction. When a stoichiometry of 1:3 is used under the same conditions, only Ln(OSi(O*t*Bu)₃)₃(η–HOSi(O*t*Bu)₃) was isolated, though in lower yield. The solid–state structures for both

siloxides were determined by X–Ray crystallography and are shown in Figure 1. The compounds are isostructural, and the metals are five–coordinate, the silanol behaving as a bidendate ligand through lone pairs from the –OH and the –O*t*Bu groups.
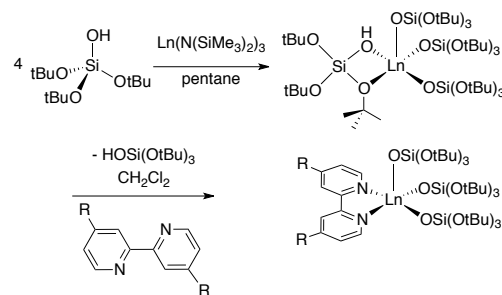
Scheme 2: Synthesis of molecular precursors Ln(OSi(O*t*Bu)₃)₃(η–HOSi(O*t*Bu)₃) (Ln = Y or Yb) and subsequent synthesis of the bipy based molecular models, where the bipy ligands are DEAS and 4,4'–Me₂bipy.

The ¹H NMR spectra of Y(OSi(O*t*Bu)₃)₃(η–HOSi(O*t*Bu)₃) in toluene d₈ is concentration dependent and gives rise to two resonances at δ_H = 1.51 and δ_H = 1.54 ppm in an area ratio of 20 : 1 (Figure S8), the minor species is not detected in the ¹³C NMR (Figure S9). At low concentration (2 mM) the minor species increases while the signal of the major species decreases and shifts to slightly lower field (*ie.* towards free silanol, Figure S10). These results suggest a dissociative equilibrium between Y(OSi(O*t*Bu)₃)₃(η–HOSi(O*t*Bu)₃) ⇌ Y(OSi(O*t*Bu)₃)₃ + HOSi(O*t*Bu)₃. Consistent with this proposal, adding an equivalent of silanol to a solution of complex causes the disappearance of the resonance at δ_H = 1.54 and an upfield shift of the δ_H = 1.51 ppm towards the free ligand. (Figure S11). When the temperature is lowered to – 40°C a resonance due to the free silanol appears at δ_H = 1.45 ppm (Figure S12). From the concentration dependence of Y(OSi(O*t*Bu)₃)₃(η–HOSi(O*t*Bu)₃) in toluene d₈ solution we can estimate that the binding of silanol to Y(OSi(O*t*Bu)₃)₃ is roughly 100.

The ¹H NMR spectra of Yb(OSi(O*t*Bu)₃)₃(η–HOSi(O*t*Bu)₃) also show two broadened resonances, associated with two types of O*t*Bu groups in a ratio of 95: 5 at 20°C at 50 mM concentration attributed to Yb(OSi(O*t*Bu)₃)₃(η–HOSi(O*t*Bu)₃) and Yb(OSi(O*t*Bu)₃)₃, respectively as proposed for the corresponding Y–complexes (Figures S13–S14).
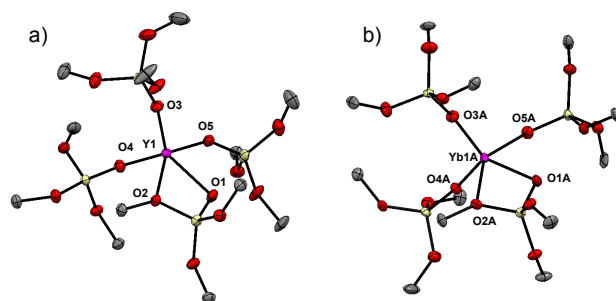
Figure 1: a) Single crystal structure of Y(OSi(O*t*Bu)₃)₃(η–HOSi(O*t*Bu)₃); b) Yb(OSi(O*t*Bu)₃)₃(η–HOSi(O*t*Bu)₃) (right), ellip-

soids at 50% of probability. Hydrogen atoms and methyl (*t*Bu) groups are omitted for clarity.

The addition of bipyridine ligands to Ln(OSi(O*t*Bu))₃(η–HOSi(O*t*Bu)) in CHCl₃ results in the displacement of HOSi(O*t*Bu)₃ and coordination of the ligand. The silanol was removed by vacuum sublimation, and the resulting residue was crystallized from CHCl₃. The bipyridine adducts were isolated in good yields (77–81%). For diamagnetic yttrium compound, the ¹H and ¹³C NMR spectra for 4,4'–Me₂bipy or DEAS adducts are consistent with a 1:1 stoichiometry in which the O*t*Bu groups are equivalent at 20 °C (Figures S15-18). At –90°C the peak corresponding to the –O*t*Bu groups broaden (Δ (RT)= 3 Hz to Δ (–90°C)= 7 Hz), and lowering the temperature to –120°C results in further broadening without resolution into two distinct signals (Figure S19).

The ¹H NMR spectra for the ytterbium compounds are broad and resonances are paramagnetically shifted (Figures S20 and S21); the chemical shifts are given in the experimental section. The IR spectra of Ln(OSiO*t*Bu)₃(DEAS) and Ln(OSiO*t*Bu)₃(4,4'–Me₂bipy), in KBr shows a blue shift of the C=C band of 14 cm⁻¹ (1591 cm⁻¹) and 27 cm⁻¹ (1616 cm⁻¹), with respect to the free ligand (1577 cm⁻¹ for DEAS and 1589 cm⁻¹ for 4,4'–Me₂bipy), in good agreement with the values obtained for the surface species (Figures S6 and S22).

The X–ray structures of the 4,4'–Me₂bipy adducts are shown in Figure 2. The solid-state crystal structures of Ln(OSi(O*t*Bu))₃(η–HOSi(O*t*Bu)) and Ln(OSi(O*t*Bu))₃(4,4'–Me₂bipy) allow us to evaluate the change in geometry around the Ln(OSi(O*t*Bu))₃ core as the bidendate ligand is changed from HOSi(O*t*Bu)₃ to 4,4'–Me₂bipy. The relevant distances and angles are listed in Table 3, and further crystallographic information is available in the supporting information. The geometries of the HOSi(O*t*Bu)₃ and 4,4'–Me₂bipy adducts of both metals are similar, as expected on the basis of the close similarity in the metal radii. The geometry is more or less a square pyramid, where the ligands in the basal plane are nitrogen from 4,4'–Me₂bipy or oxygen from η–HOSi(O*t*Bu)₃. The other two oxygen atoms of the basal planes and the apical oxygen are from –OSi(O*t*Bu)₃ groups. In all cases, the four ligands in the basal plane are bent away from the apical ligand. The dihedral angle would be 0° for an ideal square based pyramid, where the central atom is in the same plane of the ligands. In the case of the Ln(OSi(O*t*Bu))₃(η–HOSi(O*t*Bu)) the dihedral angles between the planes defined by the O1–Ln–O2 atoms and O4–Ln–O5 are 61.° for Y and 67° for Yb, leading a strong distortion, while in the case of the 4,4'–Me₂bipy adducts the angle between the planes defined by the N1–Ln–N2 and O1–Ln–O2 atoms are 42° for Y(OSiO*t*Bu)₃(4,4'–Me₂bipy), and 40° for Yb(OSiO*t*Bu)₃(4,4'–Me₂bipy). In general the apical M–O

distance is shorter than those of the basal plane, as usually observed in square pyramidal geometries.

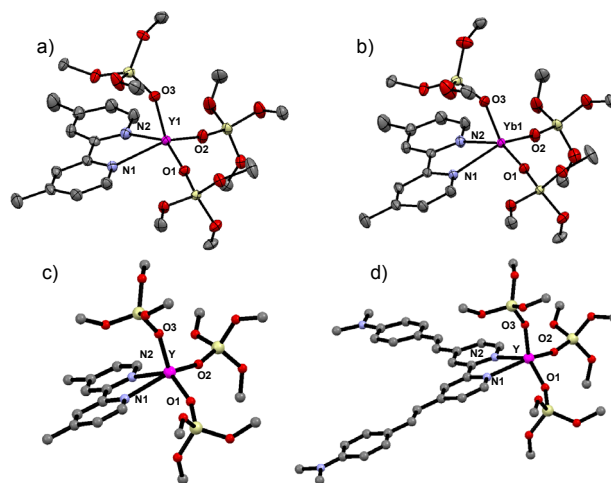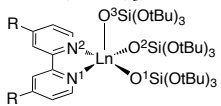**Figure 2:** a) Single crystal structure of Y(OSiO*t*Bu)₃(4,4'–Me₂bipy); b) Yb(OSiO*t*Bu)₃(4,4'–Me₂bipy), ellipsoids are shown at 50% probability, hydrogen atoms and methyl (*t*Bu) groups are omitted for clarity; c) calculated structure of Y(OSiO*t*Bu)₃(4,4'–Me₂bipy) and d) Y(OSiO*t*Bu)₃(DEAS).

DFT calculations were carried out on the molecular analogues, in particular because no suitable crystals could be grown for the DEAS derivatives. First, the calculated structure for Ln(OSi(O*t*Bu))₃(4,4'–Me₂bipy) has a similar geometry to that found experimentally in the solid state and with almost identical distances and angles of the single crystal structure (Table 3 and Figure 2). The calculated ΔG₂₉₈ of reaction for Ln(OSi(O*t*Bu))₃(η–HOSi(O*t*Bu)) with 4,4'–Me–bipy to give Ln(OSi(O*t*Bu))₃(4,4'–Me₂bipy) are –11.0 kcal/mol , and –11.9 kcal/mol for Yb and Y, respectively (*vide infra*), consistent with an exoergic binding of the bipyridine derivatives to the metal center. The DEAS adduct shows similar behavior in terms of energetics and structural features with slightly longer Ln–N bonds (Ln = Y; 2.528 vs. 2.514; Ln = Yb; 2.537 vs. 2.475 Å respectively).

These molecular studies show that lanthanide siloxides favorably bind bipyridines to yield the corresponding mono-adducts that were fully characterized by IR and NMR spectroscopies, diffraction studies and their geometries computed with DFT methods. In view of the close similarities of IR and NMR data obtained for the molecular and surface species, it is thus possible to ascertain the structure of the surface species at a molecular level, with Ln surface sites bound to a bipyridine ligand.

Table 3: Summary of the bond angles and distances from X–Ray crystallography and DFT calculations.

Complex	Dist (Å)					Angles (°)		
	Ln–O¹	Ln–O²	Ln–O³	Ln–O⁴	Ln–O⁵	O¹–Ln–O²	O²–Ln–O³	O⁵–Ln–O¹

Compound	Ln–N^1	Ln–N^2	Ln–O^1	Ln–O^2	Ln–O^3	O^1–Ln–O^2	O^1–Ln–N^1	O^2–Ln–N^2
Y(OSi(OtBu)$_3$)$_3$(η^2–HOSi(OtBu)$_3$)	2.357(3)	2.510(3)	2.081(3)	2.139(3)	2.140(3)	58.4(1)	97.1(1)	79.2(1)
Yb(OSi(OtBu)$_3$)$_3$(η^2–HOSi(OtBu)$_3$)	2.344(4)	2.472(3)	2.060(4)	2.095(4)	2.044(4)	59.6(1)	95.6(1)	79.9(1)
Y(OSi(OtBu)$_3$)$_3$(4,4'–Me$_2$bipy) [a]	2.514(4)	2. 475(5)	2.119(4)	2.119(4)	2.069(4)	107.0(1)	87.2(1)	87.6(1)
Y(OSi(OtBu)$_3$)$_3$(4,4'–Me$_2$bipy) [b]	2.537	2.540	2.125	2.132	2.090	105.70	85.57	85.30
Y(OSi(OtBu)$_3$)$_3$(DEAS) [b]	2.528	2.526	2.129	2.137	2.094	105.46	86.17	85.06
Yb(OSi(OtBu)$_3$)$_3$(4,4'–Me$_2$bipy) [a]	2.466(5)	2.446(6)	2.083(4)	2.096(4)	2.041(7)	106.9(2)	86.6(2)	87.7(2)
Yb(OSi(OtBu)$_3$)$_3$(4,4'–Me$_2$bipy) [b]	2.52	2.52	2.10	2.11	2.07	105.40	85.60	85.60
Yb(OSi(OtBu)$_3$)$_3$(DEAS) [b]	2.51	2.51	2.11	2.12	2.07	104.60	86.60	85.00

a) From the single crystal. b) from calculations.

2.3 Photophysical properties.

DEAS is known to display a charge transfer transition (CT) that is due to the diethylamino donation to the pyridyl acceptor; which is responsible for the absorption, emission, and nonlinear optical properties of related complexes.[37–38,55] This transition is absent in 4,4'–Me$_2$bipy.

The photophysical studies of the molecular model complexes Ln(OSi(OtBu)$_3$)$_3$(4,4'–Me$_2$bipy) and Ln(OSi(OtBu)$_3$)$_3$(DEAS) were examined in the solid state and in dilute pentane, toluene or dichloromethane solution. These measurements were compared to the surface species that were acquired in the solid state.
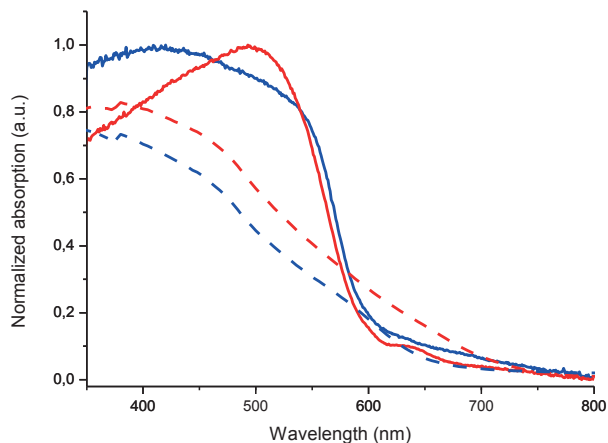

Figure 3: Solid state absorption spectra of Yb(OSi(OtBu)$_3$)$_3$(DEAS) (red solid) Y(OSi(OtBu)$_3$)$_3$(DEAS) (blue solid) [DEAS•Ln@SiO$_2$] nanoparticles Ln = Y (blue dashed), Ln = Yb (red dashed).

In the solid state Y(OSi(OtBu)$_3$)$_3$(DEAS) has an absorption maximum at 450 nm, while the maximum is red–shifted to 465 nm for Yb, corresponding to a bathochromic shift of 40 and 55 nm for each respective lanthanide (Figure 3). In dichloromethane solution Ln(OSi(OtBu)$_3$)$_3$(DEAS) display an absorption maximum and extinction coefficient [λ$_{max}$; ε] at [405 nm; 60600 M^{-1}·cm^{-1}] and [412 nm; 68000 M·cm^{-1}] for Y

and Yb, respectively, corresponding to a much smaller bathochromic shift of 6 and 13 nm relative to free DEAS than found in the solid–state. Ln(OSi(OtBu)$_3$)$_3$(4,4'–Me$_2$bipy) (Ln = Y and Yb) show similar behavior: [308 nm ; 16700 M·cm^{-1}] and [283 nm ; 16800 M·cm^{-1}] for Y and Yb, respectively. The smaller bathochromic shift observed in solution for the Ln(OSi(OtBu)$_3$)$_3$(DEAS) complexes prompted us to determine the binding constant of bipyridyl ligands to Ln(OSi(OtBu)$_3$)$_3$(η–HOSi(OtBu)$_3$).

Titrating a solution of the bipyridyl ligand with a solution of Ln(OSi(OtBu)$_3$)$_3$(η–HOSi(OtBu)$_3$) shows clear isobestic points independent of ligand and precursor combination (Figure S23) and indicates that the species involved are related linearly by stoichiometry. Using the method of continuous variation (Job's plots) we found a 1:1 stoichiometry for binding of a bipyridyl ligand to Ln(OSi(OtBu)$_3$)$_3$(η–HOSi(OtBu)$_3$).[56] The binding constants are calculated using a one–site binding model (eq. 6), where B$_{max}$ indicates the saturation point of the curve and K$_D$ the dissociation constant; the binding constant (K$_a$) is the inverse of K$_D$ (eq. 7). Plots for K$_a$ determination and Job's Plot are shown in Figures S24 and S25.

Table 4: extinction coefficients and equilibrium constant for the molecular models

Compound	λ$_{max}$ (nm)	ε (M·cm^{-1})	K$_a$[b]
DEAS	403	40000	–
4,4'–Me$_2$bipy	283	16300	–
Y(OSiOtBu)$_3$)$_3$(DEAS)	408	60600	3.6(2)x10
Yb(OSiOtBu)$_3$)$_3$(DEAS)	436	68000	18(4)x10
Y(OSiOtBu)$_3$)$_3$(4,4'–Me$_2$bipy)	308	16700	0.4(3) x10
Yb(OSiOtBu)$_3$)$_3$(4,4'–Me$_2$bipy)	308	16800	2.8(9)x10
[DEAS•Y@SiO$_2$][a]	440	–	1.7x10

a) λ$_{max}$ is calculated from recording the UV–Vis spectrum in solid state for [DEAS•Y@SiO$_2$]. b) the binding is given at T= 298K

6

$$y = \frac{B_{max}x}{1+K_D} \qquad (6)$$

$$K_m = 1/K_a \quad (7)$$

The binding constants of DEAS to "Ln(OSi(OtBu))$_3$" (Table 4) is about an order of magnitude greater than for Me$_2$–bipy, and the binding of bipyridyl ligands to Yb is about an order of magnitude stronger for Y. These data indicate a dissociation equilibrium in organic solvents. We also determined the binding of DEAS to [Y@SiO] by titration of DEAS versus a constant quantity of [Y@SiO]. The resulting curve was fitted with the same one–site binding model and gives a binding constant close to that found for the molecular analogues (1.7x10^5, Table 4, Figures S26 and S27).

The luminescence properties of the model complexes were studied both in the solid state and in solution, and compared to those of the surface derivatives (Figures S28 and S29). Irradiation of Y(OSi(OtBu))$_3$(DEAS) at 440 nm in the solid state results in the appearance of an intense emission band assigned to a ligand CT fluorescence at 585 nm (Figure 4). In pentane irradiation at 400 nm blue shifts this transition to 465 nm, with a second peak at 430 nm, a sign of presence of free DEAS due to the reversible coordination of DEAS as discussed above. In the case of Yb(OSi(OtBu))$_3$(DEAS) solid state measurements show that a similar transition is observed but with very weak intensity (Figure 4). This quenching is explained by energy transfer to the lanthanide excited state sensitizing the characteristic Yb(III) luminescence composed of four bands partially overlapped and assigned to the $^2F_{5/2} \to ^2F_{7/2}$ transitions. The additional band at higher energy, called a "hot band" at 940 nm (noted * in Figure 4a) is attributed to emission from higher crystal–field sub level of the excited state. The thermally populated hot band disappears at 77 K, and the Yb(III) emission spectrum is better resolved with four transitions at 982, 1016, 1047 and 1075 nm that correspond to the degeneracy of the $^2F_{7/2}$ ground state due to crystal–field effects. This result allows us to establish the energy splitting diagram of the M$_J$ levels and to estimate the total splitting to be ca. 880 cm^{-1}. This behavior is identical for Yb(OSi(OtBu))$_3$(DEAS) and for Yb(OSi(OtBu))$_3$(4,4'–Me$_2$bipy) in the solid state (Figures S30–S32).
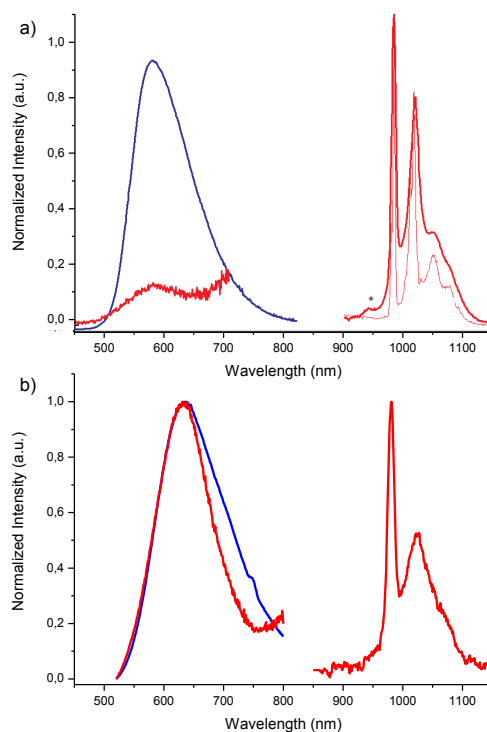

Figure 4: a) Solid state emission spectra of Ln(OSi(OtBu))$_3$(DEAS) (Ln = Y (blue); Yb (red)) zoom x 200; normalized NIR emission measured at room temperature (thick red) (* designed the hot band) and 77K (thin red). b) Solid state emission spectra of [DEAS•Ln@SiO] nanoparticles. Ln = Y (blue line), Ln = Yb (red line). λ$_{exc}$ = 400 nm .

In solution a similar behavior is observed, but due to the relatively low binding, a peak in the free DEAS region is also visible. It is well established that the splitting of the M$_J$ state is strongly correlated to the symmetry of the coordination polyhedron, and therefore an identical splitting indicates a similar structure for all molecular complexes. The total splitting value (Δ = 880 cm^{-1} for Yb(OSi(OtBu))$_3$(DEAS) in the solid state) is very high and consistent with the low symmetry coordination (see supporting information for a representation of the M$_J$ splitting, Figure S32). Finally the lifetime of the Yb(III) excited state was determined for all molecular complexes in solution and in the solid state (Table 5). In each case a perfect mono–exponential decay (eq 8) is observed with a lifetime between 5 and 5.8 μs (Figures S33 and S34).

The luminescence properties of the [DEAS•Ln@SiO] nanoparticles are shown in Figure 4. The CT emission is centered at 635 nm (+/–3nm) for both compounds, a value significantly red–shifted compared to the molecular models (Δλ$_{em}$ = 50 nm). In the case of [DEAS•Yb@SiO], additional characteristic Yb(III) NIR emission is observed in the NIR spectral range. The spectrum presents the same profile as the molecular compound but it remains quite broad even at low temperature suggesting the presence of several emitting species whose symmetry is close to that of the model compound. The lifetime of [DEAS•Yb@SiO] is not well described by a mono–exponential decay (eq. 8), which is likely due to the presence of several Yb(III) emitting sites at the surface

(Figure 4). A bi–exponential model (eq. 9) provides a better fit, with two different lifetimes τ_1 = 6 µs (40%) and τ_2 = 1.3 µs (60%). Though the bi–exponential fit is reasonable, a more realistic description is to assume a distribution of Yb(III) emitting sites at the surface of the nanoparticle, and to fit the distribution of lifetime decays by a stretched exponential model (eq. 10, Figure S35).[44,45] This model provides a distribution of decay times centered around τ_1 with a width proportional to 1/β. The dispersion factor β is dimensionless and varies between 0 and 1. β–Values close to unity indicate a narrow dispersion of sites that would resemble monoexponential decay. The integration of the function gives the first moment of time <τ>, the average time constant (eq 11), that can also been expressed as the quotient of the τ_1 and the distribution by a gamma function divided by the distribution (eq 12). The quantity <τ> is the mean relaxation time. This model is frequently used in disordered solids such as pyrene dyes grafted on alumina surfaces,[46] and more recently to understand the TEMPO radical distribution in mesoporous silica materials.[47] It is particularly interesting because it describes a distribution (β) of lifetimes centered at τ_1 which correspond to a distribution of sites on the surface.[48]

$$y = A_1 e^{-x/\tau_1} + y_0 \qquad (8)$$

$$y = A_1 e^{-\frac{x}{\tau_1}} + A_2 e^{-\frac{x}{\tau_2}} + y_0 \qquad (9)$$

$$y = A_1 e^{(-x/\tau_1)^\beta} + y_0 \qquad (10)$$

$$\langle \tau \rangle = \int A_1 e^{(-x/\tau_1)^\beta} \, dx \qquad (11)$$

$$\langle \tau \rangle = \frac{\tau_1}{\beta} \Gamma \frac{1}{\beta} \qquad (12)$$

In the present case, an excellent fit was obtained with a τ_1 of 1.7 ms, and β = 0.55, which reveals a broad distribution of sites. The corresponding <τ> is equal to 2.9 µs (Table 5, Entry 3), which is close, albeit lower to that found for the molecular species, showing that relaxation process are faster for surface species, probably because of the close proximity of the DEAS ligands. The efficiency of the metal centered luminescence (η) can be estimated using the $\eta = \tau_{obs}/\tau_r$ relationship, where τ_{obs} is the experimental lifetime of the Yb(III) and τ_r the purely radiative lifetime (0.27 ms for Yb(III)). This value allows a raw estimation of the metal centered luminescence quantum yield to 1.1%.

Finally, the two–photon cross–section of a [DEAS•Ln@SiO] nanoparticle is estimated using an additive model of the two–photon cross section of a soluble molecular model.[24,25,26] For practical reason, this experiment cannot be carried out using air and moisture sensitive Ln(OSi(OtBu))$_3$(DEAS) and consequently we use the value obtained for the tris–β–diketonate analogues Ln(TTA)(DEAS) where TTA stand for 2–thenoyltrifluoroacetonate.[27] Both Yb and Y complexes present identical two–photon absorption spectra with a maximal cross–section of 230 +/– 20 GM at 830–850 nm. Using the additive approximation for a particle

which supports ca. 180 DEASLn complexes, the two–photon cross section of the [DEAS•Ln@SiO] nanoparticles can be estimated to ca. 41.4 x 10^3 GM, falling in the same range as other doped or grafted nano–objects and quantum dots.[48,75]

2.4 Microscopy.

The particles are densely functionalized with luminescent molecular species, and it is possible to investigate these materials using two–photon microscopy imaging, using an excitation wavelength of 720 nm. The images are obtained by dispersing [DEAS•Y@SiO] or [DEAS•Yb@SiO] on a microscope coverslip. We use small amounts of dispersed material with a sufficient dilution in order to separate the particles from each other with an interparticle–distance larger than 1 µm. TEM (Transmission Electron Microscopy) microscopy of dispersed material show small aggregates of 1–2 nanoparticles (15-20 nm) to 6 nanoparticles (40-50 nm) (Figure S40). Similarly, dynamic light scattering experiments of dispersed solutions show a maximum at 38.9 nm, consistent with small aggregates of [DEAS•Ln@SiO] (Figure S41).

Figure 5a shows two–photon excited images obtained for [DEAS•Y@SiO] detected around 610 nm, as well as [DEAS•Yb@SiO] detected around 610 or 1000 nm using a microscopic set–up allowing detection at lower energies than the laser excitation.[76] Isolated spots are clearly visible with a width of about 300 nm, characteristic of the diffraction limit size of the microscope set–up. This is consistent with physical sizes or particles below ~ 50nm, sizes above this limit leading indeed to an enlargement of the imaging spot. Occasionally larger spots were detected, due to aggregation of particles during the deposition process: these spots were systematically rejected for further analysis. To evaluate the average efficiency of the particles (such as shown in the isolated spots of Figure 5b), the intensities from about 100–200 particles (taken in about 10 images) are collected using an automatic identification of isolated spots of diameter below 6 pixels. The resulting intensity histograms (Figure 5b) show a relatively good homogeneity of the particles efficiency and reflect their reasonable size dispersion, the observed intensities varying by up to a factor of two within the observed population (the intensity is indeed proportional to the number of molecules in the focal volume). The presence of various sizes, still below the limit imaging size below 50nm, is thus expected in the optical microscopy samples. The optical measurements are therefore a reasonable approach to evaluate the averaged efficiency of deposited particles which average size seems to correspond well to the objects observed in TEM.

Table 5: Emission and lifetime of molecular and surface lanthanides in solution or in solid state.

Entry	Compound	measurement	λ_{em} (vis) [nm]	λ_{em} (NIR) [nm]	Δ (NIR) [cm^{-1}]	τ_{em} (NIR) [μs]
1	[DEAS•Y@SiO$_2$]	solid–state	632	–		
2	[DEAS•Yb@SiO$_2$]	solid–state	635	981		2.9[a]
3	Yb(OSi(OtBu)$_3$)$_3$(DEAS)	solid–state	582	982	880	5[b]
		toluene (10^{-5} mM)	523	983	790	6.4[b]
4	Y(OSi(OtBu)$_3$)$_3$(DEAS)	solid–state	579	–	–	–
		pentane (10^{-5} mM)	464/490	–	–	–
5	Yb(OSi(OtBu)$_3$)$_3$(4,4'–Me$_2$bipy)	solid–state	338	983	860	5.8[b]
		pentane (10^{-5} mM)	325	984	800	6.6[b]

a) First moment of time according to equation 12, τ_r=1.9 μs; b) according to equation 8

Averaged efficiencies are 19.3 x 10 photons/s for [DEAS•Y@SiO] (610nm) and 24.4 x 10 ph/s for [DEAS•Yb@SiO] (610nm), for an incident intensity at the focal spot of 6 x 10 W/cm. The efficiencies measured for these particles are very close to the ones found in previously developed Zn(DEAS) particles, in which there is a similar number of sites per particles. Under such low excitation conditions the particles are easily detected, and do not exhibit any visible photobleaching. For comparison, 20 nm fluorescent nanospheres (yellow–green (505/515) FluoSpheres, Invitrogen) emit an average signal of 30 x 10 ph/s for the same incident intensity conditions and adequate spectral excitation/ detection conditions. Finally at 1000 nm (in the NIR), 33.6 x 10 ph/s were collected on average for [DEAS•Yb@SiO] particles. The signal to noise ratio at this wavelength is still good, even though the detectors are less efficient at this wavelength.

Figure 5: a) Two–photon fluorescence images of luminescent nanoparticles excited at 760 nm, detected at 610 nm for [DEAS•Y@SiO2] (top); [DEAS•Yb@SiO] (middle); and 1000 nm detection for [DEAS•Yb@SiO2] (bottom). b) corresponding statistics over about 200 particles and zoom on nanoparticles (pixel size : 60nm). Incident intensities: 4x10 W/cm (610nm detection) and 6x10 W/cm (1000nm detection).

3 Conclusions

Silica nanoparticles with ca. 180 emitting surface Yb(III) DEAS species absorb and emit in the NIR range with giant two–photon cross–sections (40 x 10 GM). This level of brightness allows for the detection of very small nanoparticle aggregates (*ca.* 15 to 20 nm from TEM) using NIR–to–NIR confocal biphotonic microscopy. Detailed characterization by EXAFS, IR, solid–state NMR of the diamagnetic yttrium derivative and UV–Vis established the structure of [(≡SiO)Yb(DEAS)]. Complementary studies of Ln(OSi(OtBu))(DEAS) as molecular mimics of the surface environment revealed that these models reproduce the properties found for [(≡SiO)Ln(DEAS)] in terms of binding constants (ca. 10) and photophysical properties of the surface species, supporting the structural assignment of the surface species. The luminescence lifetime in [(≡SiO)Yb(DEAS)] is best represented as a distribution of sites and the lifetime is slightly shorter than found in the molecular equivalents, which is probably due to the heterogeneity of the amorphous silica surface environment. The molecular approach presented here provides a 'road–map' towards the preparation of luminescent nano–objects using SOMC that allows direct comparison of structure – luminescence properties, thus paving the way for the design of improved nanoparticles for in–depth imaging of thick tissues. Further works are currently underway in this direction.
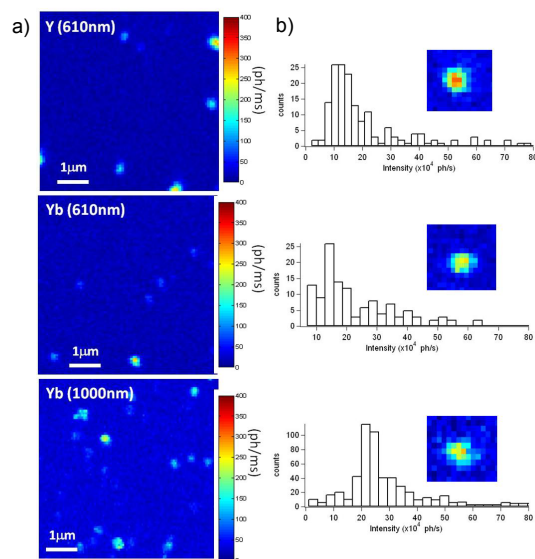
4 Experimental section

General considerations. All the experiments were carried under dry, oxygen free argon using Schlenk and glove box techniques for the organometallic synthesis. For the syntheses and the treatment of the surface species, reactions were carried out using high vacuum lines (10 mbar) and glove box techniques. Dichloromethane, pentane and toluene were purified using a double MBraun SPS alumina column, degassed before use, and stored over 4Å molecular sieves. Hexamethyldisiloxane (HMDSO) was distilled from calcium hydride and stored on molecular sieves. Deuterated solvents were directly distilled by vacuum transfer into a J–Young NMR tube. Toluene d, and CD were stored on sodium and benzophenone, CD$_2$Cl$_2$ was stored on P$_2$O$_5$ and degassed before use. The yttrium and ytterbium amides Ln(N(SiMe$_3$))$_3$ were synthesized modifying a procedure reported in literature. Silica (AEROSIL 200 m^2/g) was dehydroxylated according a published procedure. All infrared (IR) spectra were recorded using a Bruker α spectrometer placed in the

glovebox equipped with OPUS software. Typically 32 scans were accumulated for each spectrum. All the UV–Visible spectra were recorded in CH$_2$Cl$_2$ solution using quartz Schlenk cuvettes with a Cary 5000 UV–Vis–NIR spectrometer at 600 nm/min with a resolution of 1 nm. The ^{1}H, ^{13}C, and ^{29}Si–NMR spectra were obtained on Bruker DRX 200, DRX 250, DRX 300, DRX 400 or DRX 500 spectrometers. The solution spectra were recorded in the given solvent at room temperature. The ^{1}H and ^{13}C chemical shifts were referenced relative to the residual solvent peak. For the solid–state spectra, a Bruker DRX 400 was used. The MAS frequency was set at 10 kHz for all ^{1}H and ^{13}C spectra and 5 kHz for ^{29}Si. The samples were introduced in a 4 mm zirconia rotor in the glove box. ^{1}H, ^{13}C and ^{29}Si chemical shifts were referenced to external TMS.

X–Ray crystallography. The crystals were placed in paratone and mounted in the beam under a flow of nitrogen at 100 K on a Bruker SMART APEX II diffractometer equipped with a CCD area detector using Mo K$_\alpha$ radiation. Empirical absorption correction was performed with SADABS–2008/1 (Bruker). The structures were solved by direct methods (SHELXS–97) followed by least–square refinement (SHELXL–97) using WinGX suite of programs and OLEX2–1.1. The non–hydrogen atoms were refined anisotropically. The hydrogen atoms were placed at calculated positions. Additional crystallographic information are given in the Supporting Information (Table S1, Figures S36-39).

EXAFS spectroscopy. Samples were loaded into an aluminum holder equipped with aluminized Mylar windows sealed with an indium gasket in an argon–filled inert atmosphere glovebox. Assembled holders were sealed in glass jars until just prior to data collection. At the beamline, the jar was opened and the sample was quickly transferred to a helium filled cryostat, which was evacuated then refilled with helium gas three times. Data was obtained at room temperature (the cryostat was only used to provide additional oxygen protection). X–ray absorption data were obtained at beam line 4–1 of Stanford Synchrotron Radiation Light source. The X–ray beam was monochromatized using a double crystal monochromator with Si(220), ϕ=90 crystals. The second crystal was detuned by 50% to reduce the harmonic content of the beam. Data was obtained in transmission at the Yb L$_3$–edge using nitrogen–filled ion chambers and at the Y K–edge using argon–filled ion chambers. Data were deglitched using the EXAFSPAK suite of programs written by Graham George. Data were treated to remove the pre– and post–edge backgrounds and the EXAFS were obtained by subtracting a spline from the absorption data using the software package Athena. In the case of the Y K–edge data, the EXAFS contained a large, sharp feature at 7 Å^{-1} presumably due to a multi–electron excitation.

The feature was removed analogously to the process for deglitching the data — a fourth–order polynomial was fit though the data on either side of the feature and the distorted area of the EXAFS spectrum was replaced by the polynomial. EXAFS data were fit using the software package Artemis using theoretical scattering curves generated by Feff7. The number of first shell neighbors was fixed at 3, and the number of second shell neighbors was varied until the best fit was obtained. In the case of Yb@SiO$_2$, there appears to be another shell of atoms further from the Yb center; however, attempts to fit this feature using Si, O, N, C, or Yb neighbors resulted in an increase in the value of reduced χ^2, so this shell was not fit.

Transmission Electron Microscopy. The sample was ground mechanically, sonicated for 30 minutes in isopropanol and dispersed on a TEM grid. TEM pictures were obtained on a Phillips CM12 transmission electron microscope. The filament used to generate the electron beam is a tungsten filament and the accelerating voltage is 120 kV. Images were required at 100 000s time magnification.

Luminescence spectroscopy. The luminescence spectra were measured using a Horiba–JobinYvon Fluorolog–3® spectrofluorimeter, equipped with a three slit double grating excitation and emission monochromator with dispersions of 2.1 nm/mm (1200 grooves/mm). The steady–state luminescence was excited by unpolarized light from a 450 W xenon CW lamp and detected at an angle of 90° for diluted solution measurements or at 22.5° for solid state measurement (front face detection) by a Peltier–cooled red–sensitive Hamamatsu R2658P photomultiplier tube (300–1010 nm). Spectra were reference corrected for both the excitation source light intensity variation (lamp and grating) and the emission spectral response (detector and grating). Uncorrected near infra–red spectra were recorded at an angle of 45° using a liquid nitrogen cooled, solid indium/gallium/arsenic detector (850–1600 nm). The luminescence decay of ytterbium complexes was performed using an home–made set–up:. The excitation of the Yb(III) luminescence decays was performed with an optical parametric oscillator from EKSPLA NT342, pumped with a pulsed frequency tripled YAG:Nd laser. The pulse duration was 6 ns at 10 Hz repetition rate. The detection was performed by a R1767 Hamamatsu photomultiplier through a Jobin – Yvon monochromator equipped with a 1 µm blazed grating. The signal was visualized and averaged with a Lecroy digital oscilloscope LT342.

Two–Photon Microscopy Imaging. The sample was ground mechanically, vortexed and dispersed on a microscope coverslip. The two–photon excitation microscope is based on an excitation source from a Ti:Sa laser (pulse width, 100 fs; repetition rate, 80 MHz) set at a wavelength of 760 nm, focused on the sample using a water immersion high numerical aperture objective (NA 1.15, 40) after reflection on a protected silver mirror. Images are formed by galvanometric scanning (typically 10 µm x 10 µm regions are scanned, sampled with

60nm per pixel, with integration time 100μs) in the sample plane. The fluorescence emission is collected by the objective and passes through in the epi descanned detection path before being reflected by a dichroic mirror (FF720–SDi01, Semrock). Remaining laser light is further rejected by interferential filters (610/70nm or 1000/50nm) and the emission is finally focused on an avalanche photodiode working in the photon–counting mode. The lateral resolution of the imaging setup is about 300 nm.

Computational details: Computational details. All DFT calculations were performed with Gaussian 03.[?] Calculations were carried out at the DFT level of theory using the hybrid functional B3PW91.[?] Geometry optimizations were achieved without any symmetry restriction. Calculations of vibrational frequencies were systematically done in order to characterize the nature of stationary points. Stuttgart effective core potentials and their associated basis set were used for silicon, Yttrium and Ytterbium. The basis sets were augmented by a set of polarization functions (ζ=0.284 for Si and ζ=1.0 for Y and Yb). Hydrogen, Carbon, Nitrogen and Oxygen atoms were treated with 6–31G(d,p) double–ζ basis sets.[?]

Preparation of [Y(N(SiMe)₃)@SiO₂]. A representative procedure is as follows: a mixture of 2.00 g of dehydroxylated silica (SiO₂) (0.52mmol isolated SiOH, 1 equiv) and 325 mg (0.57 mmol, 1.1 equiv of Y(N(SiMe)₃)₃ was stirred in pentane at room temperature for 3 h. The reaction mixture was filtered, and the solid residue was washed five times with pentane (18 mL) and dried under high vacuum (10⁻⁵mbar) at room temperature for 1h, yielding a white solid. ¹H MAS NMR (400 MHz) δ/ppm 0.14, –0.17, and –0.55. ¹³C CP MAS NMR (100 MHz) δ/ppm 1. ²⁹Si CP MAS NMR (80 MHz) δ/ppm 16, 5, –11, –93,–101 ppm. IR ν(CH) = 2951, 2900 cm⁻¹. Elemental analysis: Y = 1.83 %, C = 3.64 %, N = 0.64 %.

Preparation of [Yb(N(SiMe)₃)@SiO₂]. This material was prepared using the procedure described above with Yb(N(SiMe)₃)₃ (373 mg, 0.57 mmol, 1.1 equiv). IR ν(CH) = 2951, 2900 cm⁻¹. Elemental analysis: Yb = 3.95 %, C = 3.55 %, N = 0.76 %.

Preparation of [Y@SiO₂]. A representative procedure is as follows: the white [Y(N(SiMe)₃)@SiO₂](1g, 0.21 mmol Y) was heated at 500°C at a heating rate of 5 K/min for 12 h at 10⁻⁵mbar. ¹H MAS NMR (400 MHz) δ/ppm 0.05 (OSiMe₃). ¹³C CP MAS NMR (100 MHz) δ/ppm 0 (OSiMe₃). IR ν(OSiMe₃) = 2963, 2905 cm⁻¹. Elemental analysis: Y = 2.10 %, C = 1.36 %, N = 0.40 %.

Preparation of [Yb@SiO₂]. The sample was prepared as described above. IR ν(SiMe) = 2963, 2905 cm⁻¹. Elemental analysis: Yb = 2.10 %, C = 1.36 %, N = 0.40 %.

Preparation of [DEAS•Y@SiO₂]. A mixture of 0.50 g of [Y@SiO₂] (0.10 mmol, 1 equiv) was reacted in dichloromethane with 55 mg (0.105 mmol, 1 equiv) of DEAS for 4 h. The solid became immediately orange. After 3 h, the solid was washed 5 times with CH₂Cl₂, and the residue

was dried at 10⁻⁵ mbar. ¹H MAS NMR (400 MHz) δ/ppm 7.3, 6.6, 3.1, 1.2. ¹³C CP MAS NMR (100 MHz) δ/ppm, note the maxima are reported: 156, 154, 149, 129, 121, 109, 45 , 13, 0 (SiMe). IR: ν(C = C) 1591 cm⁻¹. Elemental analysis: Y = 2.05 %, C = 4.72 %, N = 1.01 %.

Preparation of [DEAS•Yb@SiO₂]. This material was prepared as described above. IR: ν(C = C) 1591 cm⁻¹. Elemental analysis: Yb = 3.97 %, C = 4.72 %, N = 0.99 %.

Preparation of Y(OSi(OtBu)₃)₃(η₂–HOSi(OtBu)₃). To a solution of 2.00 g of Y(N(SiMe)₃)₃ (3.38 mmol, 1.0 equiv) in 20 mL of CH₂Cl₂ a solution of 4.0 g of silanol (7.6 mmol, 4 equiv) in 20mL of CH₂Cl₂ was added. After stirring for 8h, half of the solvent was evaporated under reduced pressure, and the solution was cooled at –40°C, after one day large transparent blocks were obtained. The crystals were collected by filtration, dried under reduced pressure and stored under argon. Yield: Y = 75 % (2.70 g). ¹H–NMR (400 MHz, toluene d₈) δ/ppm 1.55 and minor species (7 %): 1.58. ¹³C NMR (100 MHz, toluene d₈) δ/ppm 73.1 (Cₒ), 31.8 (CH₃). Anal. Calcd for C₄₈H₁₀₈O₁₆Si₄Y C = 50.41%, H = 8.81% found C = 50.38% H = 8.81%.

Preparation of Yb(OSi(OtBu)₃)₃(η₂–HOSi(OtBu)₃). The compound was prepared in 72 % yield using the procedure above with Yb(N(SiMe)₃)₃ (2,00 g, 3.04 mmol, 1 equiv). ¹H–NMR (250 MHz, C₆D₆) δ/ppm 1.60 (Δ₁/₂ = 472 Hz, tBu); minor species (5 %) and at –7.64 (Δ₁/₂ = 1309 Hz, tBu). Anal. Calcd for C₄₈H₁₀₈O₁₆SiYb C = 46.96%, H = 8.95% found: C = 46.52% H = 8.85%.

Preparation of Y(OSi(OtBu)₃)₃(DEAS). To a solution of 0.50 g (0.44 mmol, 1.0 equiv) of Y(OSi(OtBu)₃)₃(η₂–HOSi(OtBu)₃) in 20 mL of CH₂Cl₂ 222 mg of DEAS (0.44 mmol, 1 equiv) in 20 mL of CH₂Cl₂ was added. After 8h, the solvent was removed under reduced pressure, and the HOSi(OtBu)₃ was removed by sublimation at 40°C under 10⁻⁵ mbar. The resulting material was dissolved in CH₂Cl₂ and concentrated until a fine orange precipitate began to form. This solution was stored at –40°C overnight, and the solid was collected by filtration, washed with 10 mL of hexamethyldisiloxane and dried under reduced pressure. The yield was 81% (503 mg). ¹H–NMR (300 MHz, C₆D₆) δ/ppm 10.05 (d, J = 5.5Hz 2H), 7.65 (d, J = 5.8 Hz, 2H), 7.69 (s, 2H), 6.76 (d, J = 15.7 Hz, 2H), 7.37 (d, J = 8.1 Hz, 2H), 6.55 (d, J =8 Hz, 2H), 7.40 (d, J = 4 Hz, 2H), 2.93 (m, J = 6.7 Hz, 2H), 0.86 (t, J = 5.7 Hz, 2H), 1.61 (s, 81 H). ¹³C NMR (75 MHz, C₆D₆). 153.8, 150.1, 149.5, 148.6, 135.6, 129.2, 122.9, 120.5, 119.6, 117.4, 111.6, 71.5, 44.6, 32.6, 12.8. IR: ν(C = C) 1591 cm⁻¹. Anal. calcd C₆₄H₁₂₀N₂O₁₃SiₐY C = 60.84%, N = 4.05% H = 8.68% found: C = 60.35%, N = 4.02%, H = 8.65%.

Preparation of Yb(OSi(OtBu)₃)₃(DEAS). The compound was prepared in 78% yield using the procedure described above starting from 0.50 g (0.40 mmol) of *Yb(OSi(OtBu)₃)₃(η₂–HOSi(OtBu)₃)* and 201 mg (0.40 mmol) of DEAS. ¹H–NMR (200 MHz, C₆D₆) δ/ppm –0.74 (Δ₁/₂ = 97 Hz, 81 H, tBuO), 57.8 (Δ₁/₂ = 352 Hz, 2 H, ArH); 19.2 (Δ₁/₂ =

11

250 Hz, 2 H, ArH; –38.8 ($\Delta_{\nu_{1/2}}$ = 252 Hz, 2 H, ArH). IR: ν(C = C) 1618 cm^{-1}. Anal. calcd C$_{45}$H$_{77}$N$_2$O$_3$SiYb C = 56.91%, N = 3.82%, H = 8.18% found: C = 57.35%, N = 3.82%, H = 8.15%.

Preparation of Y(OSi(OtBu)$_3$)$_3$(4,4'–Me$_2$bipy). The compound was prepared in 77% yield using a similar procedure used for the preparation of the DEAS complex from 1.00 g (0.88 mmol, 1 equiv) of YOSi(O*t*Bu)$_3$)$_2$(η–HOSi(O*t*Bu)$_3$) and 4,4'–Me$_2$bipy (162 mg, 0.88 mmol, 1 equiv). ^{1}H–NMR (500 MHz, C$_6$D$_6$) δ/ppm = 9.89 (d, J = 5.4Hz, 2H), 7.14 (d, J = 4.1 Hz, 2H), 7.06 (s, 2H), 1.81 (s, 6H), 1.56 (s, 81H); ^{13}C NMR (125 MHz, C$_6$D$_6$) δ/ppm 154.2, 153.3, 151.4, 126.3, 121.4, 71.5, 32.6, 21.6. IR: ν(C = C) 1618 cm^{-1}. Anal. calcd C$_{48}$H$_{93}$N$_2$O$_9$Si$_3$Y C = 54.21%, N = 2.63%, H = 8.81% found: C = 54.35%, N = 2.68%, H = 8.81%.

Preparation of Yb(OSi(OtBu)$_3$)$_3$(4,4'–Me$_2$bipy). The compound was prepared in 78% yield (728 mg) using the procedure described above starting from 1.00 g (0.81 mmol, 1 equiv) of YbOSi(O*t*Bu)$_3$)$_2$(η–HOSi(O*t*Bu)$_3$) and 4,4'–Me$_2$bipy (149 mg, 0.81 mmol, 1 equiv). ^{1}H NMR (250 MHz, C$_6$D$_6$) δ/ppm 57.2 ($\Delta_{\nu_{1/2}}$ = 41.4 Hz, 2 H), 9.9 ($\Delta_{\nu_{1/2}}$ = 44 Hz, 6H), –0.54 ($\Delta_{\nu_{1/2}}$ = 109 Hz, 27 H) and – 107.1 ($\Delta_{\nu_{1/2}}$ = 217 Hz, 2 H). IR: ν(C = C) 1618 cm^{-1}. Anal. calcd C$_{48}$H$_{93}$N$_2$O$_9$Si$_3$Yb C = 50.24%, N = 2.44%, H = 8.17% found: C = 49.97%, N = 2.38%, H = 8.15%.

ASSOCIATED CONTENT

Supporting Information. NMR, IR and UV–Vis spectra, titrations, binding curves, lifetime measurements, crystallographic information and the full list of authors for the reference 73 are available in the supporting information.

AUTHOR INFORMATION

Corresponding Author
ccoperet@inorg.chem.ethz.ch

Present Addresses
ETH Zürich, Department of Chemistry, Wolfgang Pauli Strasse 10, CH–8093 Zürich, Switzerland

ACKNOWLEDGMENT

REFERENCES

(1) Prasad, P. N. In *Introduction to Biophotonics*; John Wiley & Sons, Inc.: **2004**, p 203.

(2) Lakowicz, J. In *Principles of Fluorescence Spectroscopy*; Lakowicz, J., Ed.; Springer US: **2006**, p 675.

(3) Nolan, E. M.; Lippard, S. J. *Acc. Chem. Res.* **2008**, *42*, 193.

(4) Kobayashi, H.; Ogawa, M.; Alford, R.; Choyke, P. L.; Urano, Y. *Chem. Rev.* **2009**, *110*, 2620.

(5) Frangioni, J. V. *Curr. Opin. Chem. Biol.* **2003**, *7*, 626.

(6) Yuan, L.; Lin, W.; Zheng, K.; He, L.; Huang, W. *Chem. Soc. Rev.* **2013**, *42*, 622.

(7) Kiyose, K.; Kojima, H.; Nagano, T. *Chem. As. J.* **2008**, *3*, 506.

(8) Nyk, M.; Kumar, R.; Ohulchanskyy, T. Y.; Bergey, E. J.; Prasad, P. N. *Nano Lett.* **2008**, *8*, 3834.

(9) Denk, W.; Strickler, J.; Webb, W. *Science* **1990**, *248*, 73.

(10) Pawlicki, M.; Collins, H. A.; Denning, R. G.; Anderson, H. L. *Angew. Chem. Int. Ed.* **2009**, *48*, 3244.

(11) Kim, H. M.; Cho, B. R. *Acc. Chem. Res.* **2009**, *42*, 863.

(12) He, G. S.; Tan, L.-S.; Zheng, Q.; Prasad, P. N. *Chem. Rev.* **2008**, *108*, 1245.

(13) Campagnola, P. J.; Loew, L. M. *Nat. Biotechnol.* **2003**, *21*, 1356.

(14) Picot, A.; D'Aléo, A.; Baldeck, P. L.; Grichine, A.; Duperray, A.; Andraud, C.; Maury, O. *J. Am. Chem. Soc.* **2008**, *130*, 1532.

(15) Zhang, T.; Zhu, X.; Cheng, C. C. W.; Kwok, W.-M.; Tam, H.-L.; Hao, J.; Kwong, D. W. J.; Wong, W.-K.; Wong, K.-L. *J. Am. Chem. Soc.* **2011**, *133*, 20120.

(16) Zhang, T.; Zhu, X.; Wong, W.-K.; Tam, H.-L.; Wong, W.-Y. *Chem. Eur. J.* **2013**, *19*, 739.

(17) Massin, J.; Charaf-Eddin, A.; Appaix, F.; Bretonniere, Y.; Jacquemin, D.; van der Sanden, B.; Monnereau, C.; Andraud, C. *Chem. Sci.* **2013**, *4*, 2833.

(18) Piszczek, G.; Gryczynski, I.; Maliwal, B.; Lakowicz, J. *J. Fluor.* **2002**, *12*, 15.

(19) D'Aléo, A.; Bourdolle, A.; Brustlein, S.; Fauquier, T.; Grichine, A.; Duperray, A.; Baldeck, P. L.; Andraud, C.; Brasselet, S.; Maury, O. *Angew. Chem. Int. Ed.* **2012**, *51*, 6622.

(20) (a) Sabbatini, N.; Guardigli, M.; Lehn, J.-M. *Coord. Chem. Rev.* **1993**, *123*, 201. (b) J.C.G. Bünzli, S. Eliseeva, J. Rare Earth, **2010**, 28, 824.

(21) Kim, S.; Pudavar, H. E.; Bonoiu, A.; Prasad, P. N. *Adv. Mater.* **2007**, *19*, 3791.

(22) Kim, S.; Pudavar, H. E.; Prasad, P. N. *Chem. Commun.* **2006**, 2071.

(23) Kim, S.; Ohulchanskyy, T. Y.; Pudavar, H. E.; Pandey, R. K.; Prasad, P. N. *J. Am. Chem. Soc.* **2007**, *129*, 2669.

(24) Wen, X.; Li, M.; Wang, Y.; Zhang, J.; Fu, L.; Hao, R.; Ma, Y.; Ai, X. *Langmuir* **2008**, *24*, 6932.

(25) Chelebaeva, E.; Raehm, L.; Durand, J.-O.; Guari, Y.; Larionova, J.; Guerin, C.; Trifonov, A.; Willinger, M.; Thangavel, K.; Lascialfari, A.; Mongin, O.; Mir, Y.; Blanchard-Desce, M. *J. Mater. Chem.* **2010**, *20*, 1877.

(26) Li, L.; Tian, Y.; Yang, J.; Sun, P.; Kong, L.; Wu, J.; Zhou, H.; Zhang, S.; Jin, B.; Tao, X.; Jiang, M. *Chem. Commun.* **2010**, *46*, 1673.

(27) Shao, G.; Han, R.; Ma, Y.; Tang, M.; Xue, F.; Sha, Y.; Wang, Y. *Chem. Eur. J.* **2010**, *16*, 8647.

(28) Rendón, N.; Bourdolle, A.; Baldeck, P. L.; Le Bozec, H.; Andraud, C.; Brasselet, S.; Copéret, C.; Maury, O. *Chem. Mater.* **2011**, *23*, 3228.

(29) Philippot, C.; Bourdolle, A.; Maury, O.; Dubois, F.; Boury, B.; Brustlein, S.; Brasselet, S.; Andraud, C.; Ibanez, A. *J. Mater. Chem.* **2011**, *21*, 18613.

(30) Zagdoun, A.; Rossini, A. J.; Gajan, D.; Bourdolle, A.; Ouari, O.; Rosay, M.; Maas, W. E.; Tordo, P.; Lelli, M.; Emsley, L.; Lesage, A.; Coperet, C. *Chem. Commun.* **2012**, *48*, 654.

(31) Copéret, C.; Chabanas, M.; Petroff Saint-Arroman, R.; Basset, J.-M. *Angew. Chem. Int. Ed.* **2003**, *42*, 129.

(32) Thomas, J. M.; Raja, R.; Lewis, D. W. *Angew. Chem. Int. Ed.* **2005**, *44*, 6456.

(33) Tada, M.; Iwasawa, Y. *Coord. Chem. Rev.* **2007**, *251*, 2702.

(34) Marks, T. J. *Acc. Chem. Res.* **1992**, *25*, 57.

(35) Wegener, S. L.; Marks, T. J.; Stair, P. C. *Acc. Chem. Res.* **2011**, *45*, 206.

(36) Liang, Y.; Anwander, R. *Dalton Trans.* **2013**, *42*, 12521.

(37) A. Hilton, T. R., O. Maury, H. Le Bozec, I. Ledoux, J. Zyss, *Chem. Commun.* **1999**, 2521.

(38) Baccouche, A.; Peigné, B.; Ibersiene, F.; Hammoutène, D.; Boutarfaïa, A.; Boucekkine, A.; Feuvrie, C.; Maury, O.; Ledoux, I.; Le Bozec, H. *J. Phys. Chem. A* **2010**, *114*, 5429.

(39) Dragonetti, C.; Balordi, M.; Colombo, A.; Roberto, D.; Ugo, R.; Fortunati, I.; Garbin, E.; Ferrante, C.; Bozio, R.; Abbotto, A.; Le Bozec, H. *Chem. Phys. Lett.* **2009**, *475*, 245.

(40) Feuvrie, C.; Maury, O.; Le Bozec, H.; Ledoux, I.; Morrall, J. P.; Dalton, G. T.; Samoc, M.; Humphrey, M. G. *J. Phys. Chem. A* **2007**, *111*, 8980.

(41) Bourdolle, A.; Allali, M.; D'Aléo, A.; Baldeck, P. L.; Kamada, K.; Williams, J. A. G.; Le Bozec, H.; Andraud, C.; Maury, O. *ChemPhysChem* **2013**, DOI:10.1002/cphc.201300501.

(42) Anwander, R.; Roesky, R. *Dalton Trans.* **1997**, 137.

(43) Gauvin, R. M.; Delevoye, L.; Hassan, R. A.; Keldenich, J.; Mortreux, A. *Inorg. Chem.* **2007**, *46*, 1062.

(44) Burkett, S. L.; Sims, S. D.; Mann, S. *Chem. Commun.* **1996**, 1367.

(45) Rataboul, F.; Baudouin, A.; Thieuleux, C.; Veyre, L.; Coperet, C.; Thivolle-Cazat, J.; Basset, J. M.; Lesage, A.; Emsley, L. *J. Am. Chem. Soc.* **2004**, *126*, 12541.

(46) Asefa, T.; Kruk, M.; Coombs, N.; Grondey, H.; MacLachlan, M. J.; Jaroniec, M.; Ozin, G. A. *J. Am. Chem. Soc.* **2003**, *125*, 11662.

(47) Bauer, J. r.; Braunschweig, H.; Dewhurst, R. D. *Chem. Rev.* **2012**, *112*, 4329.

(48) Duchateau, R. *Chem. Rev.* **2002**, *102*, 3525.

(49) Quadrelli, E. A.; Basset, J.-M. *Coord. Chem. Rev.* **2010**, *254*, 707.

(50) Edelmann, F. T.; Freckmann, D. M. M.; Schumann, H. *Chem. Rev.* **2002**, *102*, 1851.

(51) Feher, F. J.; Tajima, T. L. *J. Am. Chem. Soc.* **1994**, *116*, 2145.

(52) Cordes, D. B.; Lickiss, P. D.; Rataboul, F. *Chem. Rev.* **2010**, *110*, 2081.

(53) Fujdala, K. L.; Tilley, T. D. *Chem. Mater.* **2001**, *13*, 1817.

(54) Fischbach A., E. G., Scherer W.,Herdtweck E., and Anwander R. *Z. Naturforsch* **2004**, *59b*, 1353

(55) Sénéchal, K.; Maury, O.; Le Bozec, H.; Ledoux, I.; Zyss, J. *J. Am. Chem. Soc.* **2002**, *124*, 4560.

(56) Blanda, M. T.; Horner, J. H.; Newcomb, M. *J. Org. Chem.* **1989**, *54*, 4626.

(57) Suh, M.; Lee, H.-J.; Park, J.-Y.; Lee, U. H.; Kwon, Y.-U.; Kim, D. J. *ChemPhysChem* **2008**, *9*, 1402.

(58) Ziessel, R. F.; Ulrich, G.; Charbonnière, L.; Imbert, D.; Scopelliti, R.; Bünzli, J.-C. G. *Chem. Eur. J.* **2006**, *12*, 5060.

(59) Gonçalves e Silva, F. R.; Malta, O. L.; Reinhard, C.; Güdel, H.-U.; Piguet, C.; Moser, J. E.; Bünzli, J.-C. G. *J. Phys. Chem. A* **2002**, *106*, 1670.

(60) Reinhard, C.; Güdel, H. U. *Inorg. Chem.* **2002**, *41*, 1048.

(61) Pointillart, F.; Le Guennic, B.; Golhen, S. p.; Cador, O.; Maury, O.; Ouahab, L. n. *Inorg. Chem.* **2013**, *52*, 1610.

(62) Pointillart, F.; Guennic, B. L.; Golhen, S.; Cador, O.; Maury, O.; Ouahab, L. *Chem. Commun.* **2013**, *49*, 615.

(63) Pointillart, F.; Le Guennic, B.; Cauchy, T.; Golhen, S. P.; Cador, O.; Maury, O.; Ouahab, L. n. *Inorg. Chem.* **2013**, *52*, 5978.

(64) Chen, R. *J. Lumin.* **2003**, *102*, 510.

(65) Berberan-Santos, M. N.; Bodunov, E. N.; Valeur, B. *Chem. Phys.* **2005**, *315*, 171.

(66) Metivier, R.; Leray, I.; Lefevre, J.-P.; Roy-Auberger, M.; Zanier-Szydlowski, N.; Valeur, B. *Phys. Chem. Chem. Phys.* **2003**, *5*, 758.

(67) Gajan, D.; Schwarzwälder, M.; Conley, M. P.; Gruening, W. R.; Rossini, A. J.; Zagdoun, A.; Lelli, M.; Yulikov, M.; Jeschke, G.; Sauvée, C.; Ouari, O.; Tordo, P.; Veyre, L.; Lesage, A.; Thieuleux, C.; Emsley, L.; Copéret, C. *J. Am. Chem. Soc.* **2013**. DOI:10.1021/ja405822h

(68) Larson, D. R.; Zipfel, W. R.; Williams, R. M.; Clark, S. W.; Bruchez, M. P.; Wise, F. W.; Webb, W. W. *Science* **2003**, *300*, 1434.

(69) Pu, S.-C.; Yang, M.-J.; Hsu, C.-C.; Lai, C.-W.; Hsieh, C.-C.; Lin, S. H.; Cheng, Y.-M.; Chou, P.-T. *Small* **2006**, *2*, 1308.

(70) Clapp, A. R.; Pons, T.; Medintz, I. L.; Delehanty, J. B.; Melinger, J. S.; Tiefenbrunn, T.; Dawson, P. E.; Fisher, B. R.; O'Rourke, B.; Mattoussi, H. *Adv. Mater.* **2007**, *19*, 1921.

(71) Bradley, D. C.; Ghotra, J. S.; Hart, F. A. *J. Chem. Soc.* **1973**, 1021.

(72) Le Roux, E.; Chabanas, M.; Baudouin, A.; de Mallmann, A.; Copéret, C.; Quadrelli, E. A.; Thivolle-Cazat, J.; Basset, J.-M.; Lukens, W.; Lesage, A.; Emsley, L.; Sunley, G. J. *J. Am. Chem. Soc.* **2004**, *126*, 13391.

(73) Frisch, M. J. *Gaussian (Revision B.05),* **2003**.

(74) Perdew, J. P. *Electronic Structure of Solids*. Ed Akademie Verlag Berlin **1991**

(75) Perdew, J. P.; Burke, K.; Wang, Y. *Phys. Rev. B* **1996**, *54*, 16533.

(76) Burke, K.; Wang, Y.; Perdew, J. P. *Electronic density functional theory: Recent progress and new directions,* Ed Plenum, New York, **1997**, p11.

(77) Dobson, J. F.; Vignale G.; Mas, M. P. *Derivation of generalized Gradient approximation: The PW91 Density Functional,* **1998**.

(78) Perdew, J. P.; Chevary, J. A.; Vosko, S. H.; Jackson, K. A.; Pederson, M. R.; Singh, D. J.; Fiolhais, C. *Phys. Rev. B* **1992**, *46*, 6671.

(79) Perdew, J. P.; Burke, K.; Wang, Y. *Phys. Rev. B* **1998**, *57*, 14999.

(80)Perdew, J. P.; Chevary, J. A.; Vosko, S. H.; Jackson, K. A.; Pederson, M. R.; Singh, D. J.; Fiolhais, C. *Phys. Rev. B* **1993**, *48*, 4978.

(81) Hariharan, P. C.; Pople, J. A. *Theoret. Chim. Acta* **1973**, *28*, 213.

DISCLAIMER